Nanoscale

PAPER

View Article Online
View Journal | View Issue

Cite this: *Nanoscale*, 2024, **16**, 17412

Achieving a balance of rapid Zn^{2+} desolvation and hydrogen evolution reaction inertia at the interface of the Zn anode†

Xiaofen Xiao, *[a] Deqiang Wang,[a] Guangyi Xu,[a] Zhuxiang Zhang,[a] Jun Li,[a,b] Shun Wang, [a] Yifei Yuan,[a] Chuangang Hu [c] and Huile Jin *[a,b]

Received 9th June 2024,
Accepted 20th July 2024

DOI: 10.1039/d4nr02385d

rsc.li/nanoscale

It is difficult to achieve fast kinetics of $Zn^{2+}(H_2O)_6$ desolvation as well as HER inertia at the same electrolyte/Zn interface during long-term cycling of Zn plating/stripping in aqueous Zn-ion batteries. Herein, an effective interface construction strategy with hydrophilic transition metal oxides was proposed to achieve that balance using a CeO_2 layer coating. The hydrophilic CeO_2 layer can bring a balance between improving the access to the anode surface for $Zn^{2+}(H_2O)_6$ electrolyte ions, providing uniform Zn^{2+} nucleation sites and HER inertia. What's more, Zn corrosion can be significantly inhibited benefiting from this coating layer. The efficiency of aqueous Zn-ion batteries showed a great enhancement. Ultra-long plating/stripping stability up to 1600 h and excellent recovery (returning to 0.5 from 20 mA cm^{-2}) for the symmetric CeO_2@Zn system were observed. A full cell with the MnO_2 cathode (CeO_2@Zn//MnO_2) with good reversibility and stability (~600 cycles) was fabricated for practical application. Our work provides a fundamental understanding and an essential solution to deal with the balance between rapid desolvation and inhibition of the hydrogen evolution reaction, which is important for promoting the practical application of rechargeable Zn batteries.

1. Introduction

Among various future battery technologies beyond the lithium ion, aqueous zinc-ion batteries (ZIBs) with near-neutral electrolytes have attracted particular attention in recent years due to the following advantages: low cost, good safety, and a high abundance of Zn.[1–3] However, the great potential development of Zn metal anodes is severely hampered by the low plating/stripping coulombic efficiency (CE) and poor cycling stability caused by hydrogen evolution, corrosion and dendrite formation in slightly acidic electrolytes.[4–6] The side reactions could be expressed as follows:

$$H_2O + e^- \rightarrow \frac{1}{2}H_2\uparrow + OH^-$$

$$4Zn^{2+} + 6OH^- + SO_4{}^{2-} + nH_2O \rightarrow Zn_4SO_4(OH)_6 \cdot nH_2O\downarrow$$

The growth of Zn dendrites originated from the inhomogenous nucleation sites during the long-term cycling process, especially under large current density conditions.[7–10] What's more, Zn dendrite growth and the HER would accelerate with each other.[11] With the growth of dendrites, more active sites would be exposed and accelerate the HER rate;[12] while a rough surface would be formed on the surface of Zn as Zn corrodes in the HER.[10] This lowers the energy barrier of the desolvation process of $Zn^{2+}(H_2O)_6$ at the interface of the electrolyte/electrode to enhance a fast mass transfer kinetics of Zn plating/stripping, which is important for fostering homogeneous ion distribution and uniform deposition.[13] As reported by the research studies, hydrophilic surfaces are beneficial for driving the first trapping process of $Zn^{2+}(H_2O)_6$, however, this always occur along with solvent molecule degradation and the HER.[7]

Though various strategies have been reported on tackling these anode issues, it is still difficult to reach a certain balance between HER inertia and fast kinetics of $Zn^{2+}(H_2O)_6$ desolvation[4,10,14–17] to achieve continuous regulation of the deposition behavior of Zn during a long-term cycling process. Hence, suppressing the parasitic reaction and inducing homogeneous Zn plating/stripping at the fundamental level are urgently needed.[7,11,18]

[a]*Key Lab of Advanced Energy Storage and Conversion, Zhejiang Province Key Lab of Leather Engineering, College of Chemistry and Materials Engineering, Wenzhou University, Wenzhou, Zhejiang 325035, China. E-mail: xiaoxf3@mail2.sysu.edu.cn*
[b]*Zhejiang Engineering Research Center for Electrochemical Energy Materials and Devices, Institute of New Materials and Industrial Technologies, Wenzhou University, Wenzhou, Zhejiang 325035, China*
[c]*State Key Laboratory of Organic-Inorganic Composites, College of Chemical Engineering, Beijing University of Chemical Technology, Beijing 100029, China*
†Electronic supplementary information (ESI) available. See DOI: https://doi.org/10.1039/d4nr02385d

Analyzing the thermodynamic problems, based on the research results of the field of electrocatalysis,[19–21] the HER is a typical two-electron transfer reaction with one catalytic intermediate (H*, where * denotes a site on the electrode surface) and occurs *via* either the Volmer–Tafel or the Volmer–Heyrovsky mechanism:[22]

Volmer step:

$$H^+ + e + * \rightarrow H^* \quad (1)$$

Heyrovsky step:

$$H^* + H^+ + e \rightarrow H_2 + * \quad (2)$$

Tafel step:

$$2H^* \rightarrow H_2 + 2* \quad (3)$$

The hydrogen adsorption free energy ΔG_H above controlled the rate of the overall reaction. Based on the Sabatier's principle that the binding energy between the catalyst and the reactant should be neither too strong nor too weak, if hydrogen binds to the surface too weakly, the adsorption (Volmer) step will limit the overall reaction rate, whereas if the binding is too strong, the rate will be limited by the desorption (Heyrovsky/Tafel) step.[23,24] For 2M $ZnSO_4$ aqueous solution, it was weakly acidic because of the reaction $Zn^{2+} + 2H_2O = Zn(OH)_2 + 2H^+$.[25,26] It is very easy for (1) the Volmer step to occur because that H^+ owns an empty 1s orbital which could bind strongly with the surface O.[27] However, too much strength of the O–H bond can make the following desorption (2)/(3) (Heyrovsky/Tafel) step very difficult to occur, bringing the high energy barrier of the whole HER process. Therefore, barely transition metal oxides were used for electrocatalytic HER in acidic medium.[27,28] Here in the system of aqueous Zn-ion batteries, the HER is taken as an adverse reaction which needs to be inhibited.[12]

Based on this, CeO_2 was deliberately chosen as a coating layer to fabricate an interface bringing a balance between HER inertia and fast kinetics of $Zn^{2+}(H_2O)_6$ desolvation. On one hand, CeO_2 is a kind of typical indirect transition N-type semiconductor which is unfavorable for HER.[17,27,29,30] On the other hand, it has a hydrophilic property.[31] This gives the potential of CeO_2 that ensures a fast capture of $Zn^{2+}(H_2O)_6$ leading to a uniform distribution of Zn^{2+} nucleation sites as well as inhibiting the HER adverse reaction.[4,15,24,32] What's more, the standard electrode potential of Ce^{4+}/Ce^{3+} in aqueous solutions at 25 °C (*vs.* NHE) was much higher than $\varphi_{Zn^{2+}/Zn}$ as shown in the following:

$$Ce^{4+} + e \rightleftarrows Ce^{3+} \quad 1.72\ v$$

$$H^+ + e \rightleftarrows 1/2\ H_2 \quad 0\ v$$

$$Zn^{2+} + 2e \rightleftarrows Zn \quad -0.76\ v$$

It means that during the zinc deposition/stripping process, the CeO_2 modified layer is stable and does not allow other side reactions. Furthermore, the semiconductor CeO_2 layer can prevent the dissolution of alkaline zinc sulfate by-products into the electrolyte, slowing down the rate of corrosion on the zinc surface, which furthermore prohibits the HER.[4,16,24,32] This positive role of CeO_2 is shown in Fig. 1.

2. Results and discussion

To fabricate the coating layer, CeO_2 powder was dispersed in 4% PVDF and then drop cast onto the surface of Zn foil, NMP was removed by drying in the oven as described in the ESI.† The X-ray diffraction pattern in Fig. S1† shows the successful cast of CeO_2 without any changes in the crystal structure. Meanwhile, a small amount of PVDF here was used to guarantee the elasticity and flexibility of the coating layer as reported by our group members before.[33]

The hydrophilicity of the interface was confirmed from the contact angle measurements in 2 M $ZnSO_4$ electrolyte. As shown in Fig. 2f and g, the significantly improved hydrophilicity of the CeO_2@Zn foil anode was proved by the smaller contact angle of 60.69° compared to that of Zn foil (92.25°), that makes a great contribution to the easier desolvation process for $Zn^{2+}(H_2O)_6$ at the interface of the CeO_2 layer.

To examine the inhibitory effect on hydrogen evolution of this coating layer, CeO_2 modified on Zn foil was examined in a three-electrode system with 1 M Na_2SO_4 aqueous electrolyte, in which CeO_2@Zn foil or Zn foil was used as the working electrode, Ag/AgCl as the reference electrode, and carbon rod as the counter electrode (for more details, see the ESI†). As depicted in Fig. 2e, the LSV curves show that the overpotential for CeO_2@Zn foil to reach a current density of 20 mA cm^{-2} was ~110 mV, much higher than that of pure Zn foil, which provides direct evidence of the inhibition of the HER by the CeO_2 coating layer.

Long-term cycling stability of the symmetric batteries under different current densities and area capacities were tested as shown in Fig. 2a, b and Fig. S9–S12.† The symmetric CeO_2@Zn cells exhibited a prolonged lifespan over 1600 h (2 mA cm^{-2}, 1 mA h cm^{-2}), 750 h (5 mA cm^{-2}, 2.5 mA h cm^{-2}), 150 h (5 mA cm^{-2}, 10 mA h cm^{-2}) and 75 h (20 mA cm^{-2}, 20 mA h cm^{-2}), respectively, compared to that of the bare Zn anode at about ~360 h, ~80 h, ~20 h and ~40 h. According to the above experimental results, this might be ascribed to the stable hydrophilicity and the formation of an HER inert solid electro-

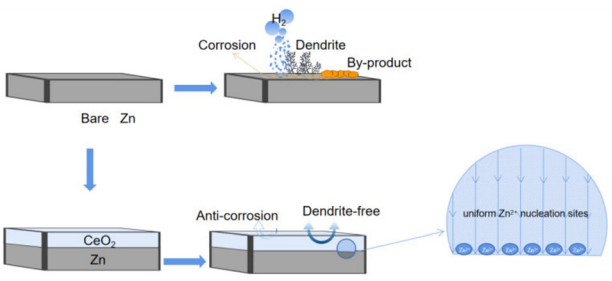

Fig. 1 Schematic diagram of the protection mechanism of the CeO_2 layer for CeO_2@Zn in Zn-ion batteries.

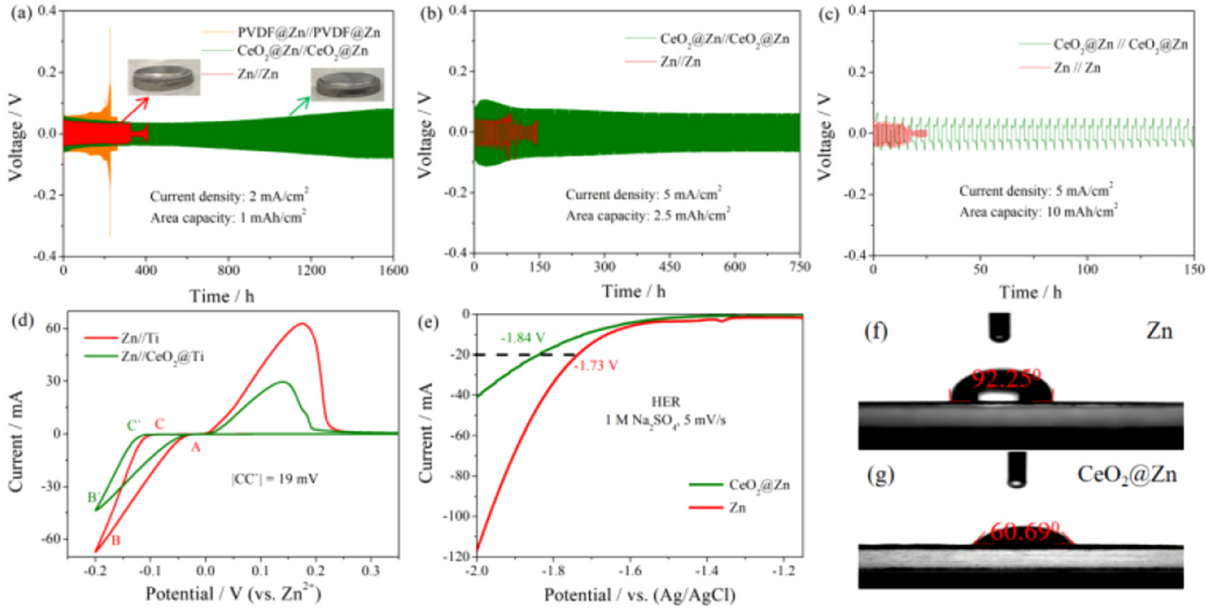

Fig. 2 Voltage profiles of symmetric cells based on Zn foil and the CeO_2@Zn anode at (a) 2 mA cm^{-2} with a capacity of 1 mA h cm^{-2}, (b) 5 mA cm^{-2} with a capacity of 2.5 mA h cm^{-2} and (c) 5 mA cm^{-2} with a capacity of 10 mA h cm^{-2}, (d) CV curves of Zn//Ti and CeO_2@Zn//Ti (0.2 mA cm^{-2} for 15 h), (e) LSV curves of bare Zn foil and CeO_2@Zn foil under a neutral electrolyte, (f) the contact angle measurement results for (g) bare Zn and (g) the fabricated Zn anodes.

lyte interface layer; all the symmetric CeO_2@Zn cells lasted longer than the symmetric bare Zn cells. The corresponding CE curves are also presented in Fig. S11–S13.†

The nucleation stage is a pivotal step for understanding the transformation course of Zn dendrite formation. The positive role played by the CeO_2 coating layer on this aspect was proven by the overpotential evolution of symmetric Zn//Zn and CeO_2@Zn//CeO_2@Zn cells at a current density of 2.0 mA cm^{-2} with a total capacity of 1.0 mA h cm^{-2} at the initial 3 cycles.[11] As can be seen from Fig. S14,† each Zn^{2+} deposition process has a typical nucleation overpotential in the Zn//Zn cell. However, there is no obvious nucleation overpotential for the CeO_2@Zn//CeO_2@Zn cell except the initial nucleation overpotential, which shows that the CeO_2 coating layer reduces the energy barrier of Zn^{2+} nucleation and changes the deposition process of Zn^{2+} compared with that of bare Zn. The positive role in inhibiting the HER played by the CeO_2 coating layer can also be proven by the phenomenon that the symmetric Zn//Zn batteries split much quickly than CeO_2@Zn//CeO_2@Zn cells because of the gas inside during long-term cycling.

Zn deposition on a foreign substrate such as bare Ti foil was investigated as shown in Fig. 2d. A crossover characteristic of nucleation processes was observed while sweeping the potential toward the positive direction and labelled as "A" in Fig. 2d, and the potential value of which is also known as the crossover potential (E_{oc}). The potential difference between the crossover point (A) and the point (B/B') where Zn^{2+} starts to be reduced on the substrate is regarded as the polarization voltage difference. No excess decomposition current on the CeO_2 interphase was observed, indicating that chemically stable films did not bring about other side reactions during cycling.[11,34]

To better understand the behavior of the CeO_2 coating layer during the Zn electrodeposition process, an optical microscope was used to monitor *in situ* the surface morphology of the dendritic growth for Zn electrodes (CeO_2@Zn and Zn). Homemade optical cells were fabricated with a transparent glass plate and 10 mA cm^{-2} was applied to the cells as shown in Fig. 3 and the ESI.† It can be seen from Fig. 3a that Zn dendrites were distributed randomly on the bare Zn surface after 10 min, and formed tree-like Zn dendrites after 30 min deposition. These

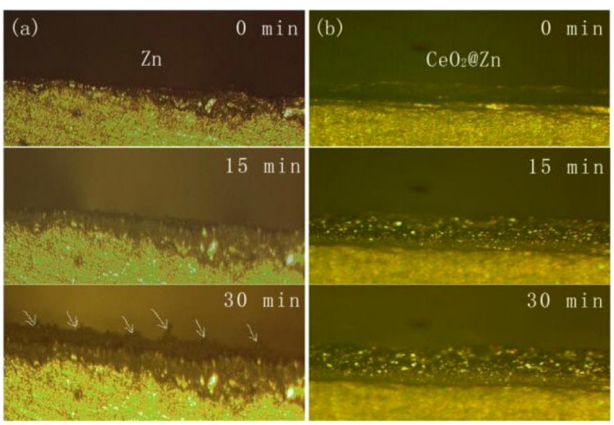

Fig. 3 Optical microscope images of (a) bare Zn and (b) CeO_2@Zn in the aqueous $ZnSO_4$ electrolyte to characterize the dendrite growth during plating at a current density of 10 mA cm^{-2}.

Zn dendrites cannot be reused and might puncture the diaphragm. The formation of these fragile dendrites (dead Zn) resulted in short circuits during the cycling stability test for Zn//Zn symmetry cells (Fig. 2a–c and Fig. S5, S9, and S10†). In contrast, it could be observed through the *in situ* deposition video (Fig. 3b and ESI video 1 and 2†) that CeO_2 uniformly covered the surface of Zn foil at the beginning; Zn^{2+} tended to electrodeposit above the surface of Zn but under the CeO_2 layer when the voltage was applied, which prevented $Zn_4SO_4(OH)_6{\cdot}nH_2O$ from dissolving into the electrolyte. This could also be proved from the XRD patterns of bare Zn and CeO_2@Zn after 250 cycling tests as seen from Fig. 5. The CeO_2 layer pushed slowly and evenly with no observed dendrites on the surface of CeO_2@Zn even after 30 min. Its uniform deposition could be attributed to the homogenization of the nucleation site by the CeO_2 layer alongside the inhibition of the HER as discussed earlier in Fig. 1.

The feasibility of CeO_2@Zn anodes in the practical application was further verified by full cells using MnO_2 as the cathode. MnO_2 was synthesized by a hydrothermal method according to a previous reports,[35] with its purity and phase state characterized by XRD as shown in Fig. S1.† The featured peaks of the sample corresponded to the standard α-MnO_2 (JCPDS: 44-0141) spectrogram, which indicated that the synthesized MnO_2 was in the α crystal phase. It indicated a nanorod morphology for the α-MnO_2 used in this experiment (Fig. S2†). For the full cell test, 0.1 M $MnSO_4$ was added to 2 M $ZnSO_4$ electrolyte to suppress the disproportion reaction of MnO_2.[35] As seen in Fig. 4a, both Zn//MnO_2 and CeO_2@Zn//MnO_2 showed the same two pairs of anodic/cathodic peaks in the CV curves derived from the two-step reverse oxidation/reduction between MOOH and MnO_2, in agreement with those reported in other literature studies.[4]

The similar CV curves of CeO_2@Zn//MnO_2 compared to that of the Zn//MnO_2 full cell revealed similar redox behavior and indicated that the CeO_2 coating layer did not affect the redox reactions in MnO_2. Furthermore, as shown in Fig. 4b the charge transfer resistance Rct value of CeO_2@Zn//MnO_2 was much lower than that of Zn//MnO_2, which indicates a more profound Zn^{2+} ion transfer at the electrolyte/anode interface of CeO_2@Zn//MnO_2, in consistence with the results of the previous contact angle test (Fig. 2f and g).

Of interest, while Zn//MnO_2 (~165 mA h g^{-1}) and CeO_2@Zn//MnO_2 (~169 mA h g^{-1}) have almost the same specific capacity for the initial discharge profile at 0.2 C (Fig. 4c and Fig. S6†), however, there is an obvious faster fading of the capacity for the uncoated Zn//MnO_2 (discharge capacity ~120 mA h g^{-1}) at the second discharge step compared to CeO_2@Zn//MnO_2 (discharge capacity ~159 mA h g^{-1}). The possible mechanism was controversial and has been deeply discussed by researchers in recent years.[4]

H^+ plays a vital role for the charge storage mechanism in our rechargeable Zn//MnO_2 system, and our experimental results can be explained according to the H^+ conversion reaction mechanism reported recently.[4] For the first discharge step, MnO_2 reacts with a proton from water to form MnOOH ($MnO_2 + H^+ + e^- +$ MnOOH) in both cells, since the electrolyte was the same for both Zn//MnO_2 and CeO_2@Zn//MnO_2 at the beginning. Counter to the H^+ ions reacting with MnO_2, the resulting OH^- ions reacted with $ZnSO_4$ and H_2O in the aqueous electrolyte to form large flake-like $ZnSO_4[Zn(OH)_2]_3{\cdot}xH_2O$ and reached a neutral charge in the system. As

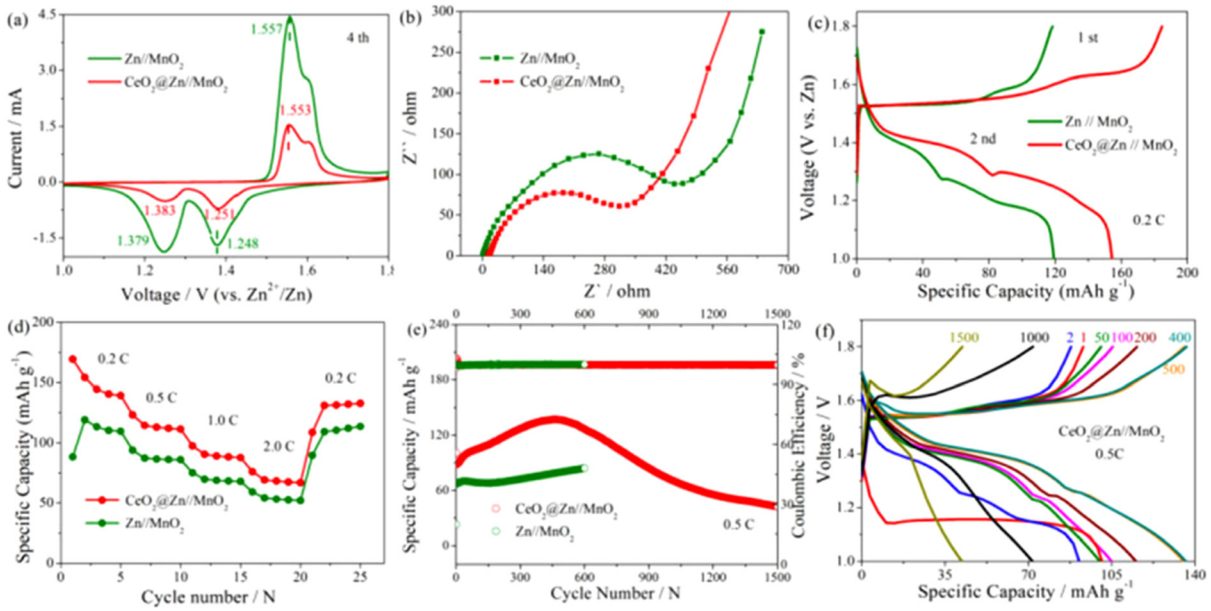

Fig. 4 Performance of Zn/MnO_2 and CeO_2@Zn//MnO_2 batteries: (a) CV curves at a scanning rate of 0.1 mV s^{-1}, (b) Nyquist plots, (c) DC curves at 0.2 C derived from (d) rate performance at various current densities, (e) cycling performance at 0.5 C and (f) DC curves derived from (e).

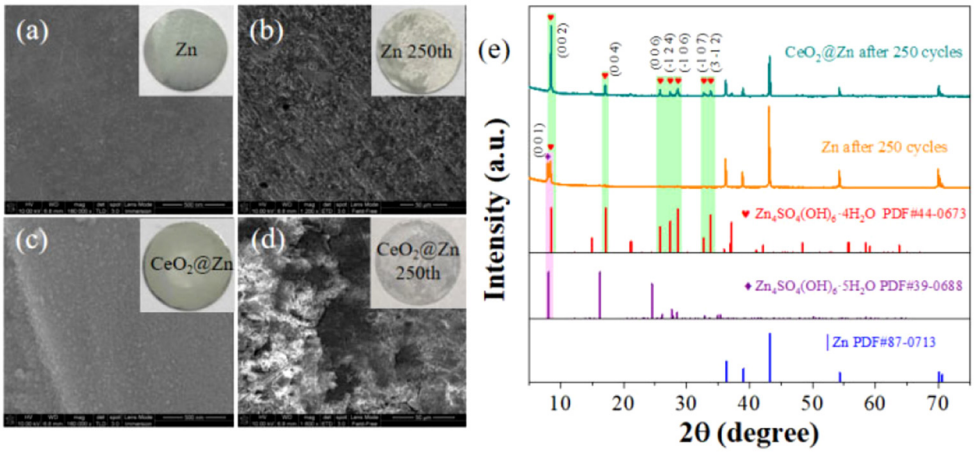

Fig. 5 SEM photos of : (a) Zn and (b) Zn after 250th cycles, (c) CeO_2@Zn and (d) CeO_2@Zn electrode after 250th cycles, respectively; (e) the XRD patterns of the corresponding electrodes in (a).

shown in Fig. 2e, the coating layer of the anticatalytic HER CeO_2, thereby alleviating H^+ to form H_2 and promoting the formation of MnOOH. This supports the longer cycling stability and shorter decreasing of specific capacity for CeO_2@Zn//MnO_2 compared to that of Zn//MnO_2 observed in Fig. 4f.

The rate capability of full cells was evaluated at current densities from 0.2 to 2.0 C (Fig. 4d and Fig. S5†). It was observed that the modified CeO_2@Zn//MnO_2 showed better capacity than that of bare Zn//MnO_2 at various current densities, both of which exhibited excellent reversibility (returning to 2.0 from 0.2 C). This illustrates the high feasibility of this energy storage system. The long-term cycling performance of full cells (CeO_2@Zn//MnO_2 and Zn//MnO_2) was tested at 0.5 C between 1.0 and 1.8 V (Fig. 4e). For CeO_2@Zn//MnO_2, the capacity gradually increased with every activation before 500 cycles, but then gradually decreased since ~500 laps and led to 30% capacity retention rate after 1500 cycles. However, the capacity of Zn//MnO_2 steadily lasted around 600 cycles and then cut off.

To further validate our analysis on the performances above, we disassembled the tested batteries and analyzed their structures and morphologies. Scanning electron microscopy (SEM) images revealed the surface morphology of the bare Zn and CeO_2@Zn anodes in the symmetric cells before and after cycling (Fig. 5a–d). Initially, the bare Zn anode exhibit a smooth and shiny metallic sheen surface (Fig. 5a), CeO_2@Zn was also smooth but with a thin layer of the CeO_2 solid covering the surface (Fig. 5c). After 250 cycles, a layer of coarse nanoflakes covered the surface of the bare Zn layer (Fig. 5b and Fig. S4†) which was randomly distributed. However, the SEM images show that CeO_2@Zn still maintained a relatively smooth and strong solid surface with a homogeneous Zn deposition, with no tree-like nanoflakes being observed (Fig. 5d). XRD patterns have proven that the sediment on CeO_2@Zn was $Zn_4SO_4(OH)_6{\cdot}4H_2O$. In contrast, much less $Zn_4SO_4(OH)_6{\cdot}xH_2O$ (x = 4,5) was observed for bare Zn since it was dissolved in the electrolyte and this has been verified previously in the literature.[36] This intuitively proves the positive role of the CeO_2 layer in preventing zinc surface corrosion and formation of dendrites.

3. Conclusions

In summary, an efficient hydrophilic interface strategy that can bring a balance between the rapid desolvation kinetics of $Zn^{2+}(H_2O)_6$ and inhibition of the HER by CeO_2 layer coating was developed. It greatly improved the easy access of electrolyte ions to the anode surface, provided uniform Zn^{2+} nucleation sites, inhibited the HER and Zn corrosion desolvation, leading to a significant enhancement of the efficiency of aqueous Zn-ion batteries (Table S1 in the ESI†). The long-term stability of symmetrical CeO_2@Zn//CeO_2@Zn batteries was observed as they lasted for ~1600 h without obvious dendrite formation, which is almost 4.4 times than that of bare Zn//Zn. The modified CeO_2@Zn coupled with α-MnO_2 cathode presented excellent reversibility and greatly improved long cycling stability with almost no decay after 600 cycles compared with bare Zn. Our work provides a fundamental understanding and an essential solution to deal with the balance between rapid desolvation and inhibition of the hydrogen evolution reaction, which is important for promoting the practical application of rechargeable Zn batteries.

4. Experimental and methods

4.1. Chemicals

Deionized water (18.2 MΩ) was used for all experiments. Zn foil (20 μm, 80 μm, 99.9%) was bought from Guangsheng New Materials Co. Ltd. $ZnSO_4{\cdot}7H_2SO_4$ (99.0%), $MnSO_4$ and Ti foil (10 μm, 99.99%) were bought from Aladdin Reagent Co. LTD. Hydrophobic carbon paper was bought from Shanghai Hesen Electric Co., Ltd. Glass fiber membrane (Whatman GF/D, glass microfiber filters, diameter 47 mm) was brought from

Shanghai Yuling Filtering Equipment Ltd. *N*-Methyl-2-pyrrolidone (NMP, >99.5%) and PVDF (M_w = 8900–9800) were bought from Shanghai Aladdin Bio-tech Co. Ltd.

4.2. Characterization of the morphology and structure

XRD patterns were recorded using a Bruker-AXS micro-diffractometer (D8 ADVANCE) with Cu-K_α radiation (λ = 1.5406 Å) from 10° to 90°. The contact angle between the electrolyte and the Zn anode was measured using a contact angle measuring instrument (JC2000D1, Shanghai Powereach Digital Technology Equipment Co., Ltd.) An optical microscope (6XB-PC, Optical Instrument Factory) was used to observe *in situ* the deposition and exfoliation of Zn. A homemade optical cell was fabricated using Zn plates (100 mm × 100 mm × 50 mm) fixed on a transparent glass plate for the *in situ* optical analysis.

4.3. The synthesis of electrode materials

The synthesis of α-MnO_2. α-MnO_2 was synthesized according to a previous report [Nature Energy, 2016, 1, 16039], 0.5 M H_2SO_4 (2 ml) was added into 0.003 M $MnSO_4{\cdot}H_2O$ (90 ml) and magnetically stirred. Then, 0.1 M $KMnO_4$ (20 ml) aqueous solution was slowly added into the above solution. The solution was transferred to a Teflon-lined autoclave and kept at 120 °C for 12 h after being stirred for 2 h. Then the obtained material was collected by vacuum filtration and washed three times with water, and dried in a vacuum oven.

The preparation of CeO_2@Zn anode. Zn foil was polished using emery paper, and then washed with ethanol. 4 wt% PVDF was prepared by dissolving PVDF in NMP at 40 °C under magnetic stirring. CeO_2 and PVDF solution were mixed together in the ratio CeO_2 : PVDF (9 : 1) and then 100 μl of the mixture was drop cast onto Zn or Ti foil, and the resultant electrodes were dried in an oven at 80 °C, overnight to remove the NMP completely.

The preparation of the PVDF@Zn anode. All the procedures followed were the same as that for the above CeO_2@Zn foil except that CeO_2 was not added.

4.4. The assembly of batteries and electrochemical measurements

All cell measurements (galvanostatic charge–discharge, linear polarization and chronoamperograms) were performed on a Neware Battery Tester (Shenzhen, China). Corrosion analysis and cyclic voltammetry of full cells were tested at a scan rate of 0.1 mV s^{-1} and the EIS spectra were recorded on an electrochemical workstation (VMP-300, Bio-Logic Science Instruments Co.) with a frequency range from 100 kHz to 0.01 Hz using a BioLogic electrochemistry workstation.

HER measurements were conducted in a three electrode configuration, in which bare Zn and coated Zn plate were used as the working electrode, the Zn plate as the counter electrode, and saturated Ag/AgCl as the reference electrode. The corrosion potential and corrosion current were calculated from the Tafel fit system in the electrochemical workstation.

The electrochemical performance of symmetrical Zn//Zn (or CeO_2@Zn//CeO_2@ Zn) cell batteries. A symmetrical Zn//Zn cell was assembled using the cleared Zn foil (80 μm, *Φ*16 mm) as both the anode and cathode, 2 M $ZnSO_4$ as the electrolyte (200 μl) and a glass fiber membrane as the membrane (*Φ*19 mm). All coin cells used in our experiment were 2032-type. Long-term cycling was measured under (2 mA cm^{-2}, 1 mA h cm^{-2}), (5 mA cm^{-2}, 2.5 mA h cm^{-2}) (5 mA cm^{-2}, 10 mA h cm^{-2}), while for the deep-discharge tests, Zn foil was used (25 μm) under 10 mA cm^{-2}. Zn//Ti (or Zn//CeO_2@Ti) cells were tested under the current density of 5 mA cm^{-2} for 0.5 h for the CE of Zn anodes.

The electrochemical performance of Zn (or CeO_2@Zn) //MnO_2 batteries. α-MnO_2 electrodes were fabricated by mixing α-MnO_2 powder, carbon black and PVDF at a weight ratio of 7 : 2 : 1 in NMP solvent, then coating the slurry onto hydrophobic carbon paper using a razor blade. The α-MnO_2 mass loading was about 1–3 mg cm^{-2}. Zn/MnO_2 (or CeO_2@Zn//MnO_2) batteries were performed as CR2032 type coin cells with the α-MnO_2 electrodes as the cathode, glass fiber as the separator and Zn foil as the anode. The electrolyte was 2 M $ZnSO_4$ with 0.1 M $MnSO_4$ aqueous solution (200 μl) at 0.2 C with a voltage range of 1.0–1.8 V.

The calculation of DoD for full cells.[37] The formula used to calculate the DOD is as following:

$$\mathrm{DOD} = \frac{y}{C_{\mathrm{Zn,volume}} \cdot x \times 10^{-4}} \times 100\% = \frac{y}{0.585x} \times 100\%$$

where x (μm) is the thickness of the Zn foil and y (mA h cm^{-2}) represents the Zn areal capacity used in the electrochemical testing. Here the DoD was 1% as shown in Fig. 4e.

Author contributions

J. Li. and C. H. conceptualised the study. X. X. and H. J. obtained the funding. S. W. and Y. Y. provided resources. X. X., Z. Z., G. X. and D. W. conducted the experiments.

Data availability

The authors confirm that the data supporting the findings of this study are available within the article and its ESI.†

Conflicts of interest

There are no conflicts to declare.

Acknowledgements

This work was supported by the National Natural Science Foundation of China (52272088) and the China Postdoctoral Science Foundation (220708). We further thank Tingting He for the help with the schematic part in Fig. 1.

References

1 G. Fang, J. Zhou, A. Pan and S. Liang, *ACS Energy Lett.*, 2018, **3**, 2480–2501.
2 J. S. Kim, S.-W. Heo, S. Y. Lee, J. M. Lim, S. Choi, S.-W. Kim, V. J. Mane, C. Kim, H. Park, Y. T. Noh, S. Choi, T. van der Laan, K. Ostrikov, S.-J. Park, S. G. Doo and D. H. Seo, *Nanoscale*, 2023, **15**, 17270–17312.
3 Y. Du, R. Kang, B. Zhang, H. Wang, G. Chen and J. Zhang, *ACS Energy Lett.*, 2024, **9**, 967–975.
4 C. Xu, B. Li, H. Du and A. F. Kang, *Angew. Chem., Int. Ed.*, 2012, **51**, 933–935.
5 L. Cao, D. Li, T. Pollard, T. Deng, B. Zhang, C. Yang, L. Chen, J. Vatamanu, E. Hu, M. J. Hourwitz, L. Ma, M. Ding, Q. Li, S. Hou, K. Gaskell, J. T. Fourkas, X.-Q. Yang, K. Xu, O. Borodin and C. Wang, *Nat. Nanotechnol.*, 2021, **16**, 902–910.
6 J. Yin, Y. Wang, Y. Zhu, J. Jin, C. Chen, Y. Yuan, Z. Bayhan, N. Salah, N. A. Alhebshi, W. Zhang, U. Schwingenschlögl and H. N. Alshareef, *Nano Energy*, 2022, **99**, 107331.
7 L. Wang, B. Zhang, W. Zhou, Z. Zhao, X. Liu, R. Zhao, Z. Sun, H. Li, X. Wang, T. Zhang, H. Jin, W. Li, A. Elzatahry, Y. Hassan, H. J. Fan, D. Zhao and D. Chao, *J. Am. Chem. Soc.*, 2024, **146**, 6199–6208.
8 F. Bu, Z. Sun, W. Zhou, Y. Zhang, Y. Chen, B. Ma, X. Liu, P. Liang, C. Zhong, R. Zhao, H. Li, L. Wang, T. Zhang, B. Wang, Z. Zhao, J. Zhang, W. Li, Y. S. Ibrahim, Y. Hassan, A. Elzatahry, D. Chao and D. Zhao, *J. Am. Chem. Soc.*, 2023, **145**, 24284–24293.
9 Y. Xu, X. Zheng, J. Sun, W. Wang, M. Wang, Y. Yuan, M. Chuai, N. Chen, H. Hu and W. Chen, *Nano Lett.*, 2022, **22**, 3298–3306.
10 K. Liang, S. Huang, H. Zhao, W. Liu, X. Huang, W. Chen, Y. Ren and J. Ma, *Adv. Mater. Interfaces*, 2022, **9**, 2200564.
11 R. Zhao, X. Dong, P. Liang, H. Li, T. Zhang, W. Zhou, B. Wang, Z. Yang, X. Wang, L. Wang, Z. Sun, F. Bu, Z. Zhao, W. Li, D. Zhao and D. Chao, *Adv. Mater.*, 2023, **35**, 2209288.
12 X. Jia, C. Liu, Z. G. Neale, J. Yang and G. Cao, *Chem. Rev.*, 2020, **120**, 7795–7866.
13 H. Li, R. Zhao, W. Zhou, L. Wang, W. Li, D. Zhao and D. Chao, *JACS Au*, 2023, **3**, 2107–2116.
14 C. Xie, Y. Li, Q. Wang, D. Sun, Y. Tang and H. Wang, *Carbon Energy*, 2020, **2**, 540–560.
15 S. So, Y. N. Ahn, J. Ko, I. T. Kim and J. Hur, *Energy Storage Mater.*, 2022, **52**, 40–51.
16 P. Li, J. Ren, C. Li, J. Li, K. Zhang, T. Wu, B. Li and L. Wang, *Chem. Eng. J.*, 2023, **451**, 138769.
17 F. Li, D. Ma, K. Ouyang, M. Yang, J. Qiu, J. Feng, Y. Wang, H. Mi, S. Sun, L. Sun, C. He and P. Zhang, *Adv. Energy Mater.*, 2023, **13**, 2204365.
18 Q. Ren, X. Tang, K. He, C. Zhang, W. Wang, Y. Guo, Z. Zhu, X. Xiao, S. Wang, J. Lu and Y. Yuan, *Adv. Funct. Mater.*, 2024, **34**, 2312220.
19 X. Xiao, C. Hu, Q. Dai, C. Xiong, D. Liu and H. Jin, *J. Electroanal. Chem.*, 2022, **925**, 116862.
20 X. Xiao, C.-T. He, S. Zhao, J. Li, W. Lin, Z. Yuan, Q. Zhang, S. Wang, L. Dai and D. Yu, *Energy Environ. Sci.*, 2017, **10**, 893–899.
21 X. Xiao, Z. Fang and D. Yu, *Front. Mater.*, 2019, **6**, 219.
22 Z. W. Seh, J. Kibsgaard, C. F. Dickens, I. Chorkendorff, J. K. Norskov and T. F. Jaramillo, *Science*, 2017, **355**, eaad4998.
23 Y. T. Xu, X. Xiao, Z. M. Ye, S. Zhao, R. Shen, C. T. He, J. P. Zhang, Y. Li and X. M. Chen, *J. Am. Chem. Soc.*, 2017, **139**, 5285–5288.
24 H. Liu, J. G. Wang, W. Hua, H. Sun, Y. Huyan, S. Tian, Z. Hou, J. Yang, C. Wei and F. Kang, *Adv. Sci.*, 2021, **8**, 2102612.
25 T. Shoji, M. Hishinuma and T. Yamamoto, *J. Appl. Electrochem.*, 1988, **18**, 521–526.
26 P. K. Bowen, J. Drelich and J. Goldman, *Adv. Mater.*, 2013, **25**, 2577–2582.
27 J. Suntivich, K. J. May, H. A. Gasteiger, J. B. Goodenough and Y. Shao-Horn, *Science*, 2011, **334**, 1383–1385.
28 E. Skulason, T. Bligaard, S. Gudmundsdottir, F. Studt, J. Rossmeisl, F. Abild-Pedersen, T. Vegge, H. Jonsson and J. K. Norskov, *Phys. Chem. Chem. Phys.*, 2012, **14**, 1235–1245.
29 A. Vojvodic and J. K. Nørskov, *Natl. Sci. Rev.*, 2015, **2**, 140–143.
30 Y. Jiao, Y. Zheng, M. Jaroniec and S. Z. Qiao, *Chem. Soc. Rev.*, 2015, **44**, 2060–2086.
31 X. Huang, K. Zhang, B. Peng, G. Wang, M. Muhler and F. Wang, *ACS Catal.*, 2021, **11**, 9618–9678.
32 K. Wang, M. Qin, C. Wang, T. Yan, Y. Zhen, X. Sun, J. Wang and F. Fu, *J. Colloid Interface Sci.*, 2023, **629**, 733–743.
33 R. Zhao, Y. Yang, G. Liu, R. Zhu, J. Huang, Z. Chen, Z. Gao, X. Chen and L. Qie, *Adv. Funct. Mater.*, 2020, **31**, 2100445.
34 L. Ma, M. A. Schroeder, O. Borodin, T. P. Pollard, M. S. Ding, C. Wang and K. Xu, *Nat. Energy*, 2020, **5**, 743–749.
35 H. Pan, Y. Shao, P. Yan, Y. Cheng, K. S. Han, Z. Nie, C. Wang, J. Yang, X. Li, P. Bhattacharya, K. T. Mueller and J. Liu, *Nat. Energy*, 2016, **1**, 16039.
36 R. Zhao, Y. Yang, G. Liu, R. Zhu, J. Huang, Z. Chen, Z. Gao, X. Chen and L. Qie, *Adv. Funct. Mater.*, 2020, **31**, 2001867.
37 X. Zhang, L. Zhang, X. Jia, W. Song and Y. Liu, *Nano-Micro Lett.*, 2024, **16**(1), 75.

